

Qualifying Examination Part II:

**A Critical Review of: Accurate residual stress
measurement as a function of depth in environmental
barrier coatings via a combination of X-ray diffraction
and Raman spectroscopy**

By: Bryant Kanies, M.S.

**Committee Members: Drs. G. Yang, K.L. Murty,
M. Bourham, and B. Beeler**

Introduction

Many industrial processes require critical components to operate successfully for an extended period of time in harsh conditions. These conditions may include oxidizing and corrosive atmospheres, high temperatures and temperature gradients, high pressure, fluctuating cyclic stresses, radiation, and the presence of detrimental foreign debris [1], [2]. Traditional nuclear power plants, petroleum refining facilities, high-temperate fuel cells, several aerospace applications, and turbine power production may be subject to such conditions [1]–[7]. Of these conditions, high temperature is particularly noteworthy because, along with weight reduction, increased efficiency can be gained from increased operation temperature of engines, turbines, and reactors [8].

Fusion reactors are expected to operate in excess of 1000 °C, certain Generation IV (Gen IV) nuclear reactors may reach ~1500 °C, gas temperature in turbine engines could exceed 1650 °C, and several aerospace applications will require materials which can operate around 2000 °C [1], [2], [9], [10]. In this work, high temperature is generally taken to mean ≥ 1200 °C. Ni-based superalloys are typically limited to operation in temperatures ranging from 900 – 1100 °C [8], [11]–[13]. Operation at higher temperatures can lead to increased oxidation, high temperature corrosion, thermal fatigue, fatigue cracking, premature rupture, and decreased strength [1]. Ceramic materials offer promising solutions to several of these issues by maintaining satisfactory mechanical, tribological, chemical, and physical properties at elevated temperatures [8]. However, ceramic materials are typically brittle, flaw-sensitive, and lack toughness [8], [14], [15]. This lends them to catastrophic failure modes, and makes them susceptible to damage during fabrication and service [15]. To this end, ceramic matrix composites (CMCs) have been developed as potential structural component materials. CMCs are light weight, corrosion resistant, and have higher fracture toughness than monolithic ceramics [8], [14]. Furthermore, ceramic materials may be used as thermal barrier coatings (TBCs) to increase the lifetime of structural components [16]. In this case, the ceramic material is applied as a coating which serves as insulation between a high temperature process and the structural substrate [16].

Unfortunately, traditional TBC and CMC materials exhibit undesirable properties in harsh environments above ~1200 °C. Above 1100 °C, yttria-stabilized zirconia (YSZ), a typical TBC material, undergoes phase changes and is susceptible to CMAS (calcium-magnesium-alumino silicates) attack – which is discussed later [8], [17]. Non-oxide, Si-based CMCs suffer rapid recession in the presence of water vapor at temperatures above 1200 °C, which can lead to premature failure [18], [19]. Water vapor is present in many of the previously mentioned applications. Environmental barrier coatings (EBCs) have been proposed to alleviate these issues. EBCs are ceramic coatings, much like TBCs, designed to protect components from corrosive environments at high temperatures [8]. Rare earth (RE) silicates represent the most recent generation of EBCs, and are of particular importance in protecting Si-based non-oxide ceramics [12]. There are several important qualities which EBCs must be designed to have. Their coefficient of thermal expansion (CTE) must be similar to the substrate and other coating layers, and they must exhibit corrosion resistance and phase stability at their operating temperature [8]. Additionally, it is critical that EBCs maintain integrity through several thermal cycles. Failure of EBCs could lead to exposure of the underlying components, which may then lead to premature failure of the entire system. The failure of EBCs and TBCs is often attributed to their residual stress [18], [20], [21]. Thus, to reliably characterize their lifetime and performance, it is paramount to understand the residual stress in EBCs.

The work of Ye and Jiang is dedicated to such a pursuit [22]. In their work, a ‘novel’ technique combining X-ray diffraction (XRD) and Raman piezospectroscopy is developed to measure the residual stress in RE EBCs. Specifically, they measure the stress present in an ytterbium disilicate (YbDS or $\text{Yb}_2\text{Si}_2\text{O}_7$) EBC. Herein, the work of Ye and Jiang is reviewed in detail. Special focus is given to the underlying principles supporting their work. Through a critical review, several critiques and suggested improvements are offered. These focus largely on insufficient background information, reproducibility, accuracy, and the novelty of their work.

Summary of Work

In their work, Ye and Jiang first deposited the YbDS EBCs on two-dimensional (2D) carbon-silicon carbide (C/SiC) CMC substrates via the slurry coating method at Northwestern Polytechnical University. These CMCs were produced via Chemical Vapor Infiltration (CVI); they were 40x5x3.5 mm in size. A 40 μm SiC bond coat was deposited on the surface of the substrate through an unspecified manner. The EBC was 80 μm thick and consisted of 90 mass-% YbDS with 10 mass-% $\text{Ba}_{0.5}\text{Sr}_{0.5}\text{Al}_2\text{Si}_2\text{O}_8$ (BSAS or barium strontium aluminosilicate). The BSAS was added to lower the temperature required for sintering of the coating.

Following deposition, the samples were placed in an aluminum oxide (Al_2O_3) tube furnace to simulate a high-temperature, corrosive environment. This tube furnace contained 50% water vapor and 50% oxygen. The samples were kept at 1250 $^\circ\text{C}$ over the course of a 50-hour period. Following this experiment, the samples were removed from the furnace, wrapped in resin, cut with a diamond wire saw, and then polished. The saw had a downward cutting speed of 3 mm/h, and the samples were ultimately partitioned into 10x5x3.5 mm cross-section pieces. The samples were cut so that the residual stress along the depth profile could be measured through Raman piezospectroscopy. A scanning electron microscope (SEM) image of the cross section, as seen in Figure 1, was taken after partitioning.

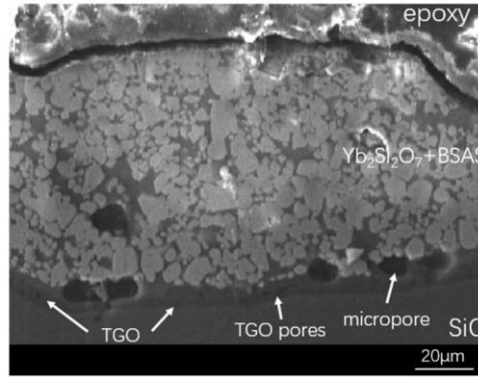


Figure 1: Cross-sectional SEM image of the YbDS + BSAS EBC system [22].

Raman Spectroscopy was then performed using a LaRAM HR Evolution HORIBA microscope with a minimum resolution of 1 μm . A 633 nm He/Ne laser was used to collect the Raman spectra. The laser was set to 25% of its maximum power to ensure that the temperature did not rise and cause errors during the measurement. This was done with the intention of obtaining a good signal-to-noise ratio and peak intensity. Additionally, the temperature was kept constant at 298 K \pm 1 K in ambient air. The spectra were measured at 5 μm intervals from the surface of the topcoat down to the interface between topcoat and thermally grown oxide (TGO). The laser was irradiated on the sample cross-sections, and three different positions were measured at each depth to establish a standard deviation. Measurements were performed exclusively in the YbDS regions because it was the main coating component. A single point was measured five times at 5 s/scan. Once obtained, the spectra were smoothed and denoised. Multi-peak fitting using Lorentz functions was then performed using the Labspec5 software. After fitting, the peak position of the 921 cm^{-1} Raman band was plotted against the distance of the scan from the surface of the EBC. In other words, the plot of the peak shift vs. depth was obtained; this can be seen in Figure 2. The original, stress-free peak position (921 cm^{-1}) was determined by performing Raman spectroscopy on YbDS powder from the same batch used for the coating.

The $\text{Sin}^2 \Psi$ method was employed next using a Bruker D8 X-ray diffractometer with a Cu target. The $[\bar{2}20]$ plane was selected due to its strong intensity and the idea that 2θ angles have higher accuracy of measured stress. To measure this plane, the detector scanned from $2\theta = 40^\circ$ to $2\theta = 55^\circ$; the diffraction peak of the $[\bar{2}20]$ plane is located at $2\theta = 47.700^\circ$. This method allows for the measurement of strain at different

tilt angles (Ψ) by using the plane as an in-situ strain gauge. The residual stress near the surface region of the coating was measured by fitting a line to the Strain vs. $\sin^2 \Psi$ plot, which can be seen in Figure 2.

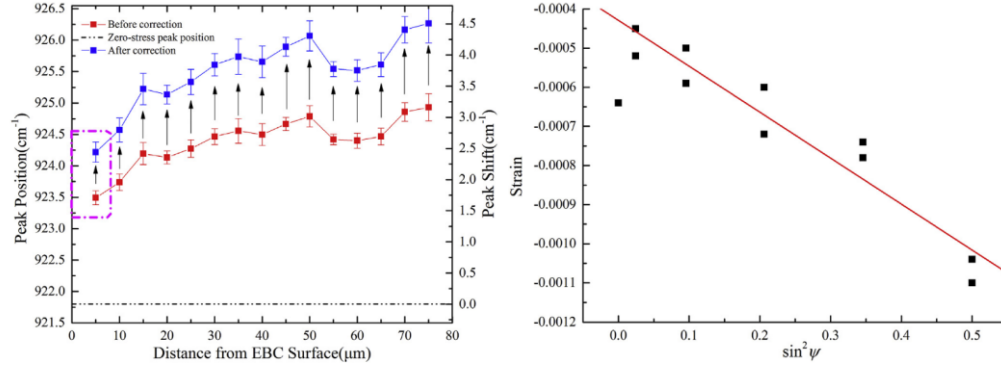


Figure 2: Left: Peak position and peak shift as a function of distance from EBC surface. Right: The resultant plot from the $\sin^2 \Psi$ method; a linear fit of this plot can be used to determine the surface stress [22].

Once the residual stress near the surface was determined using the $\sin^2 \Psi$ method, it was related to the peak shift through the following equation:

$$\Delta v_n = \frac{\Pi_n(\sigma_1 + \sigma_2 + \sigma_3)}{3} \quad (1)$$

Here, Δv_n is the peak shift, Π_n is the piezo spectroscopic (PS) coefficient, and σ_1 , σ_2 , and σ_3 represent the stress in the coating. The subscript n refers to the specific Raman peak. By solving for the PS coefficient, the stress at each depth could be determined based on the peak shift measured in the Raman spectra. Since the sectioning causes the stress normal to the cross-section to relax, the stress calculated was converted to biaxial stress through the following relationship:

$$\sigma_B = \frac{\sigma_{edge}}{1 - \nu} \quad (2)$$

Here, σ_B represents the biaxial stress, ν represents Poisson's ratio, and σ_{edge} is the measured stress on the newly exposed, free surface. The biaxial stress represents the residual stress present in the coating after fabrication and exposure to the high-temperature, corrosive environment. Once the biaxial stress was determined, the PS coefficient was recalibrated, and the true Raman peak shifts were plotted as seen in Figure 2. Finally, the residual stress profile was generated as seen in Figure 3.

Background

Ceramic Matrix Composites

CMCs consist of a ceramic matrix which is reinforced through the incorporation of fibers throughout the matrix [8], [15]. Ceramics generally have good oxidation and corrosion resistance as well as low density, thermal conductivity, and CTEs at high temperatures – making them ideal candidates for many applications [8]. Ceramics are usually ionically or covalently bonded, and may be crystalline or amorphous [23]. This type of bonding leads to low tensile strength and low toughness, or the ability to absorb energy and deform without fracturing, hence the brittle nature of ceramics [23]. Ceramics, due to their manufacturing processes, also tend to be porous. These pores may act as stress concentrators, which combine with the brittle nature of ceramics to lead to catastrophic failure [23]. Catastrophic failure occurs when a material does not undergo meaningful plastic deformation before failure. In the case of ceramics, this may mean rapid crack propagation across an entire component.

In CMCs, the matrix materials are toughened by the fibers through compressive prestressing, crack impeding, fiber pullout, crack deflection, or phase transformation toughening [15]. Compressive prestressing occurs when the CTE of the fiber is greater than that of the matrix. Cracks may be impeded when the

toughness of the fiber is greater than the local matrix. In this case, the crack may be arrested or bow out. Fiber pullout occurs when a crack propagates along the fiber/matrix interface. The fibers may remain intact while the matrix is pulled apart. In this case, fibers may bridge the gap created, allowing for continued use of the CMC, or may pull out altogether. During crack deflection, weak fiber/matrix interfaces will lead to cracks deflecting away from their principal direction due to the presence of the fiber. Finally, the stress at the crack tip may even cause a phase transformation in the fiber. This may be accompanied by a volumetric expansion which may close the crack. Essentially, a CMC allows for microcracking without catastrophic failure [15]. This effectively improves the toughness of a matrix material compared to its monolithic counterpart. As an example, a monolithic alumina sample exhibited toughness of 4-5 MPa m^{1/2} while an alumina sample with 20 volume-% SiC whiskers (short fibers) demonstrated a toughness of 8-8.5 MPa m^{1/2} [15]. Fiber aspect ratio, fiber orientation, relative moduli of fiber and matrix, matrix porosity, CTE mismatch, and flaws present in the fiber are all key metrics contributing to the performance of CMCs [15], [24].

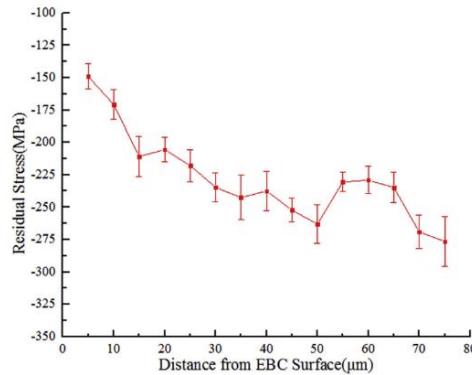


Figure 3: Plot of the residual stress present in the YbDS EBC system as a function of depth from [22].

There are several methods used to fabricate CMCs including: cold pressing and sintering, chemical vapor deposition (CVD), polymer impregnation pyrolysis, liquid or melt infiltration, hot pressing and sintering, nano infiltration and transient eutectic phase sintering, reaction bonding, directed oxidation, sol-gel, electrophoretic deposition, self-propagating high-temperature synthesis, and slurry infiltration [8], [10], [15]. In general, fabrication consists of a fiber preform being filled with appropriate reactants or materials, and then being processed with a combination of appropriate pressures and temperatures. Fiber preforms may be yarns, continuous fibers, woven fabrics, or 3D shapes. Some common types of CMCs, denoted as fiber/matrix, include: SiC/SiC, C/SiC, Al₂O₃/Al₂O₃, Nicalon/SiC, and Nicalon/nicalon glass [8], [9], [15], [22]–[25]. A plethora of fibers, ranging from ZrO₂ to Kevlar and carbon nano-tubes, exist and are in use as well [26]. In the aerospace industry, CMCs have been used in exhaust cones, outer and inner flaps, flame holders, and the nose cap of the X-38 return vehicle [8]. They have been used as shrouds, airfoils, and combustors in gas turbines, brake pads for cars, first wall blanket materials in fusion reactors, cutting tool inserts, and ceramic composite filters [8], [9], [15], [27].

Protective Coatings

Protective surface coatings are used in several applications ranging from protection of machining tools to improved corrosion resistance of nuclear fuel cladding [28], [29]. Coatings can be used to enhance corrosion and wear resistance, surface hardness, and thermal and electrical insulation amongst other things [30]. In this vein, TBCs were designed with low thermal conductivity to extend component lifetime by inhibiting the transfer of heat to an underlying substrate [8], [16], [17]. Unfortunately, these TBCs cannot withstand the desired operating conditions which are present in advanced nuclear and aerospace applications. Additionally, advanced structural materials, such as Si-based CMCs, which may circumvent the need for TBCs suffer volatilization in the same conditions.

A typical coating system consists of a ceramic topcoat, a bond coat, and the substrate material [8], [16], [18], [21]. When the substrate is metallic, a MCrAlY alloy (M = Co, Ni, Fe, or Pt) is typically used [17]. These bond coats may be formed by a combination of electro-deposition, CVD, or plasma spraying [17]. With a Si-based substrate, Si or mullite may be used as the bond coat. Mullite is a combination of alumina and silica, often denoted as $3\text{Al}_2\text{O}_3 \cdot 2\text{SiO}_2$ [31]. A thermally grown oxide (TGO) layer usually forms between the topcoat and bond coat as oxygen diffuses through the ceramic coating oxidizing the MCrAlY alloy [21]. This bond coat may lead to undesired stress and phase instability, but it may also impede the transport of oxygen or water vapor penetrating the outer coating layers [32]. Furthermore, it also consumes oxidizing species reaching the bond coat – creating a diffusion barrier which delays the transport of oxidizing species to the substrate [32]. A typical structure of a TBC can be seen in Figure 4.

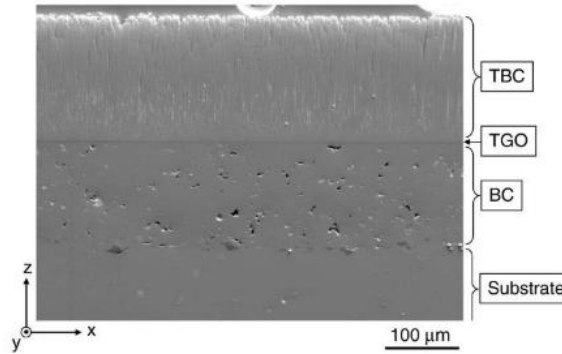


Figure 4: A 4 mole-% YSZ TBC demonstrating a typical structure from:[32].

Protective coatings may be deposited through CVD, the slurry dip/spin technique, and the sol-gel method amongst other methods [12], [33]–[39]. The slurry coating method (dip/spin) was utilized by Ye and Jiang [22]. A slurry is a mixture which consists of fine, solid particles suspended in a liquid. In the slurry coating method, the liquid solution is applied to the surface of a substrate by either dipping the substrate into the solution or pouring the solution on top. The substrate may then be spun to even out the thickness of the liquid coating precursor [33]–[39]. The slurry and substrate are then sintered following application [33]–[36].

Residual Stress in Coatings

Understanding residual stresses in EBCs is crucial for evaluating their performance and lifetime. Residual stresses influence the adhesion and tribological performance of coatings which in turn may lead to the degradation and failure of the underlying structural substrate material [40]. Stresses may lead to cracking and buckling which in turn may cause spallation and delamination. This may provide penetration pathways for oxygen, water vapor, and CMAS [18]. Therefore, it is crucial to develop reproducible techniques for the measurement and characterization of residual stresses [41], [42].

Residual stresses can be measured in a variety of ways. These include nanoindentation, layer removal, hole drilling, curvature measurements, neutron diffraction, normal and synchrotron-XRD, photo-stimulated luminescence piezospectroscopy (PLPS), and Raman piezospectroscopy [20], [31], [41]–[45]. Of these, non-destructive techniques are the most appealing because they may offer the ability to measure stresses in-situ. The curvature method is commonly applied to thin films [20], [31], [32], [46]. This method relies on Stoney's formula which is only a good approximation when the coating has uniform thickness and is much thinner than the substrate [31]. PLPS relies on the photo-stimulated luminescence of Cr^{3+} or Eu^{3+} . Cr is an impurity present in many metallic bond coats and samples containing Al, and Eu^{3+} can be added as a dopant [17], [42], [47]. This method functions very similarly to Raman piezospectroscopy, relying on the luminescent peaks of the ions.

X-Ray Diffraction – The $\sin^2 \Psi$ Technique

In X-ray diffraction (XRD), X-rays are generated and passed through divergence slits and onto a sample. The X-rays are then elastically scattered off electrons present in the sample lattice. Scattered X-rays are then collected by receiving slits, a monochromator, and a detector. The diffracted X-rays undergo constructive interference, exhibiting interference maxima, when the X-rays remain in phase [48]. The conditions which generate these maxima satisfy Bragg's law, with λ representing the wavelength of the incident radiation, d_{hkl} the lattice spacing of a particular plane, θ the diffraction angle, and n an integer [49]:

$$n\lambda = 2d_{hkl} \sin \theta \quad (3)$$

The $\text{Sin}^2 \Psi$ method takes advantage of the regularly spaced lattice planes and uses them as an in-situ strain gauge [20], [40], [48]. To understand this method, it is helpful to establish a coordinate system as that of Figure 5. Ω is the angle between the incident X-rays and the surface sample, θ is the diffraction angle, and Ψ is the angle between the normal vector of the (hkl) plane and sample surface normal vector. It is sometimes helpful to describe the lattice spacing of a certain stressed plane, d_{hkl} , in terms of its angles Φ and Ψ . Thus, $d_{\text{hkl}} \approx d_{\Phi\Psi}$. During a $\text{Sin}^2 \Psi$ measurement, a crystal plane with a high diffraction angle ($2\theta > 125^\circ$) is selected. The diffraction peaks of this plane are then acquired by adjusting the angle, Ω , between the X-ray source and the sample surface. At each Ω , the strain is determined. Ψ is then determined by subtracting the incident angle from the diffraction angle ($\Psi = \theta - \Omega$). Finally, a plot of the strain vs. $\text{Sin}^2 \Psi$ can be generated. Often one can use $d_0 = d_{\Psi=0}$, where d_0 is the unstressed lattice spacing, instead of determining d_0 . This is because the elastic strains are typically less than 0.1% which is negligible compared to instrumental errors [48]. The strain in the $\mathbf{L}_{\Phi\Psi}$ direction is expressed as [20], [40], [48]:

$$\varepsilon = \frac{d_{\phi\Psi} - d_0}{d_0} = \frac{1 + \nu}{E} \sigma_{\phi} \sin^2 \Psi - \frac{\nu}{E} (\sigma_{11} + \sigma_{22}) \quad (4)$$

In this equation, E is Young's modulus, ν is Poisson's ratio, and σ is the stress. The subscripts indicate the direction of the stresses. Upon closer examination, this equation is linear with ε and $\sin^2 \Psi$ being the dependent and independent variables, respectively. Thus, by taking a linear fit of the ε vs. $\sin^2 \Psi$ plot, the slope of the line is $(1 + \nu)\sigma_\phi/E$, which can be manipulated to determine the stress near the sample surface in the Φ direction. This method may also be applied using transmission XRD where the radius of the Debye rings are related to the lattice spacing [43].

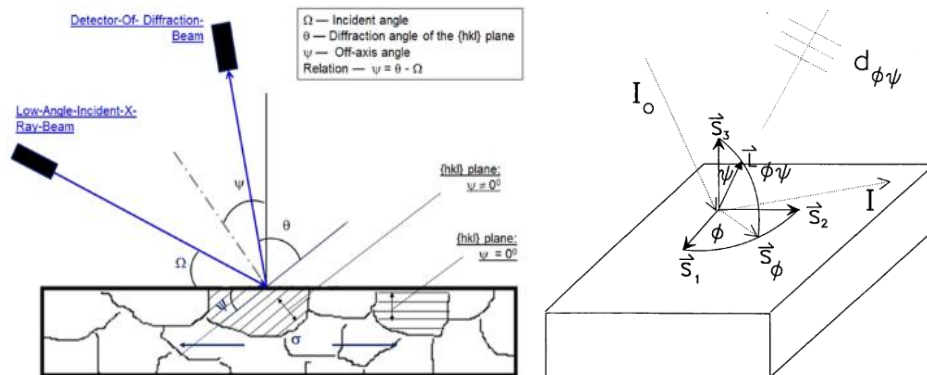


Figure 5: Coordinates describing the measurement of stress using XRD, adapted from: [40], [48]

Raman Piezospectroscopy

Raman spectra are generated by reflecting a laser off a sample and measuring the Raman shift of the inelastically scattered light. Peak position is often determined by fitting Raman spectra with Lorentzian or Gaussian functions, or a combination of the two [32], [41], [46], [50]–[53]. The piezo-spectroscopic effect is the stress-induced shift of peak frequency, or wavenumber, of the spectroscopic bands pertinent to the

material under observation [54]. Essentially, as a sample is stressed, the peak position corresponding to the maximum intensity of Raman-scattered light is shifted. This effect is captured through the following equation:

$$\Delta\nu = \Pi_{ij}\sigma_{ij} \Rightarrow \Delta\nu = \Pi\langle\sigma\rangle \Rightarrow \nu = \Pi\langle\sigma\rangle + \nu_0 \quad (5)$$

Π_{ij} is the tensor of the derivatives of the frequency shifts with respect to stresses and is also called the tensor of the piezo-spectroscopic (PS) coefficients. σ_{ij} is the stress tensor representing the stresses applied along the axes of the crystallographic system, and $\Delta\nu$ is the observed frequency shift of the peak position (peak shift). [54]. Ceramic materials most often consist of randomly distributed grains which cause the stress along crystallographic directions to be lost. Therefore, the equation can be rewritten such that Π and σ are averages for the sample. Usually, the PS coefficients are determined by a calibration procedure where the sample is stressed to a known extent and the Raman spectrum is recorded [54]. Equation 18 demonstrates that the relationship between stress and peak shift is usually linear such as is demonstrated in Figure 6 [32], [51]–[55]. The slope of this linear relationship is simply the PS coefficient. Figure 6 also demonstrates a typical setup for calibration of the PS coefficient and acquisition of a Raman spectrum.

By comparing measured Raman spectra of coating samples to calibrated PS coefficients, the residual stress in the coating can be determined. The calibration of the PS coefficient usually requires preparation of an additional, freestanding sample of the same material type as the coating [55]. The creation of a calibration system can be complicated as not many Raman microscopes can accommodate the necessary equipment [54]. Raman measurements are often limited by the penetration depth of the laser [41], [53]. Confocal Raman microscopy is promising for depth profiling of stress, and the micrometer scale of the probe size of Raman microscopy is on the order of individual grains [41], [50], [51].

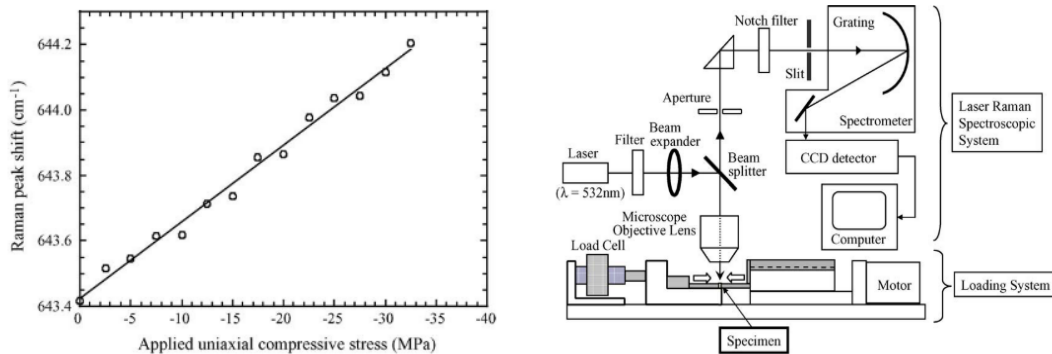


Figure 6: Left is an example of $\Delta\nu$ vs. applied stress. Right is an example of a typical calibration setup [55].

Critical Review

The work of Ye and Jiang represents a promising step towards a reliable, efficient, and widely applicable method of determining the residual stress present in protective coatings. PS coefficients have been shown to vary with thermal cycles and material content [46], [51], [53]. Thus, their proposed method of combining the $\text{Sin}^2 \Psi$ technique and Raman piezospectroscopy does represent a more efficient way to determine the residual stress in a sample. Furthermore, there is great potential for using the method in-situ. The authors do provide a straightforward, concise explanation demonstrating the need for such coating systems, but this explanation requires an extensive background to understand. For this reason, pertinent background information has been extensively reviewed. Unfortunately, there are also several issues with reproducibility and accuracy in their work. Despite its promising nature, its novelty and impact are also somewhat suspect.

Insufficient Background

Ceramic Matrix Composites: Overall, Ye and Jiang provided little background on CMCs. The previous discussion on CMCs was included in the Background section for clarity. In reality, Ye and Jiang failed to

discuss what makes CMCs promising, how they provide improved toughness, and how they are formed. More importantly, Ye and Jiang offer no explanation or insight into the CVI process used for their C/SiC CMCs. When CVD is used for large amounts of a matrix material it is called chemical vapor impregnation or infiltration (CVI) [15]. During this process, a solid material is deposited through an isothermal decomposition of gaseous reactants onto a heated substrate, which is the preform [8], [15]. This technique is usually coupled with a temperature gradient to avoid restricting gas flow to the interior of the preform. The CVI process results in CMCs with good mechanical properties at high temperatures, large, complex shapes produced in a near-net shape manufacturing process, and a diverse range of fibers and matrices that can be employed [15].

Protective Coatings: From Ye and Jiang’s paper, it is difficult to discern the difference between TBCs and EBCs. It is also difficult to see the true importance of the type of EBCs used in their study. While they mention volatilization due to water vapor and oxygen, they fail to mention its underlying mechanisms and another significant problem: CMAS attack. When used for the protection of high temperature components, EBCs and TBCs must adhere to fundamentally similar requirements. In general, EBCs distinguish themselves through improved oxidation and corrosion resistance when compared to TBCs. The fundamental requirements for TBCs and EBCs are summarized in Table 1. Most often, EBCs and TBCs are deposited through either atmospheric plasma spraying (APS) or electron-beam-physical vapor deposition (EB-PVD) [8], [17], [18]. During the APS process, a plasma gun provides a DC/induction plasma stream which can reach 10,000 K [30]. A feedstock containing the desired coating materials is fed into this high-speed plasma stream and deposited on a substrate [30]. This process can utilize several different types of feedstock such as liquids, powders, and slurries. In the EB-PVD method, an electron beam is directed onto a crucible of source material. The EB vaporizes the source material which is then directed to the substrate for coating. The vaporized source then condenses on the substrate creating a solid film/coating [30]. The EB-PVD and APS process are depicted in Figure 7. APS and EB-PVD require line-of-sight for deposition, meaning that they are not conducive for complex shaped components. Additionally, APS requires surface roughening of the substrate to promote mechanical interlocking with the coating which may reduce the fracture strength of the coated samples [35]. Slurry coating does not require line-of-sight and is generally inexpensive with limited effect on the fracture strength [35]. Unfortunately, the slurry coating technique requires high heat treatment which could lead to substrate damage [12].

Table 1: Fundamental properties required for TBCs and EBCs; adapted from: [8], [16]–[19].

Property	Purpose
High melting point	Operation in high temperature environment
Low thermal conductivity	Thermal insulation of substrate ^a
CTE match with substrate	Dissimilar expansion causes residual stress
Phase stability over operating range	Phase changes may contribute to residual stresses
Chemically inert	Oxidation and corrosion resistance ^b
Chemical compatibility with substrate	Reaction with substrate may lead to precipitates or phases with undesired properties
Low sintering rate	Densification of porous ceramic may change coating properties
Low density	Low weight is often desired in high temperature applications
^a – EBCs may not be required to serve as thermal insulators if the substrate can withstand operation temperature	
^b – TBCs may not be exposed to reactive chemicals depending on the application	

Improved resistance to volatilization, phase stability issues, and CMAS attack provide the major impetus for research into EBCs. CMAS attack is the corrosion of a material by molten calcium-magnesium-alumino silicates, or CMAS [56]. Typical TBCs deposited by atmospheric plasma spraying (APS) or electron-beam-physical vapor deposition (EB-PVD) usually have lamellar or columnar microstructures, respectively [18], [56]. These microstructures create pathways for infiltration by molten contaminants. Dust, sand,

and volcanic ash are all CMAS particles. These particles melt around 1200 °C and infiltrate the porous microstructure of protective coatings [13], [56]. When the component cools, CMAS solidifies which causes high thermomechanical stresses in the ceramic layer. These stresses may result in cracks which lead to delamination during thermal cycling. Furthermore, in YSZ-based TBCs, zirconia can reprecipitate as Y-depleted ZrO₂ grains after interaction with CMAS [56]. The destabilized zirconia is then free to undergo allotropic phase transformations during thermal cycling inducing more stress. Above 1100 °C, the t'-tetragonal phase of YSZ will change to monoclinic and cubic phases which give rise to volumetric changes. In turn, these lead to cracks in the TBC which promotes oxidation of the bond coat and growth of the TGO. This can ultimately lead to spallation of the TBC and failure of the component [8].

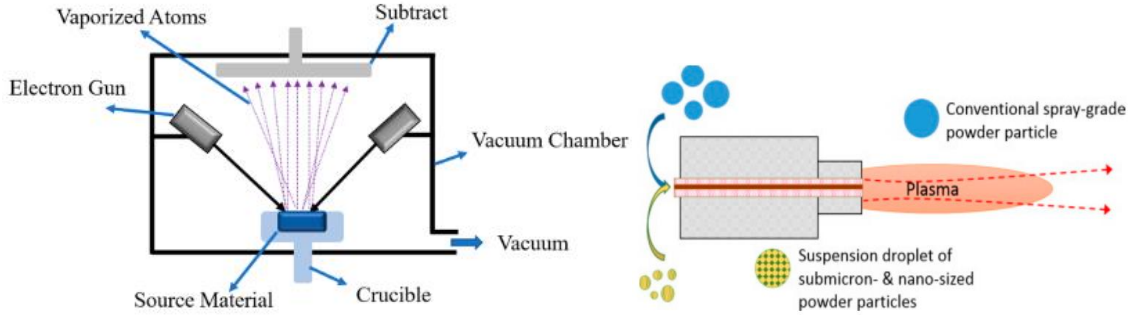
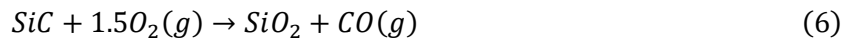


Figure 7: The EB-PVD process is depicted on the left. On the right, the APS process can be seen [30].

Si-based ceramics used for CMCs, such as SiC and Si₃N₄, form a slow growing, dense silica scale in clean, dry atmospheres. This gives them excellent oxidation resistance [19]. At temperatures greater than 1200 °C and in the presence of water vapor or alkali salts, however, this silica scale is volatilized, resulting in rapid recession of the material [18], [19]. Even in the presence of a dry atmosphere, non-oxide ceramics, such as SiC and Si₃N₄, have volatile reactions with oxygen at temperatures exceeding 1500 °C [11]. As an example, the volatile reaction of SiC in O₂ and subsequent reaction between silica (SiO₂) and water vapor is given in Equations 6 & 7 [13]. These factors clearly demonstrate the need for reliable, highly stable, corrosion resistant EBCs.



RE silicates represent the most recent generation of EBCs [12], [13]. The first generation consisted of a mullite bond layer with a YSZ top coating. It was found that mullite degrades seriously in combustion environments. This is caused by corrosion of silica from water vapor and the thermal stress generated in the EBC due to CTE mismatch of YSZ and Si-based substrates. This led to delamination of the system. The second generation consisted of a three-layered approach with a Si bond coat, a mullite or mullite and BSAS secondary coat, and a BSAS topcoat. The BSAS replaced YSZ as top coating material because of the similarity between its CTE and that of SiC. Additionally, it has a relatively low silica activity compared to mullite. BSAS, unfortunately, suffers degradation above 1400 °C so the service temperature of a Si/mullite/BSAS EBC is limited to 1300 °C. The third and most recent generation of EBCs consists of a Si bond coat, a mullite intermediate layer, and RE silicate topcoat.

Several RE silicate polymorphs are promising because they have CTE values similar to that of mullite and SiC [12], [13]. Rare earth elements consist of scandium, yttrium, and the lanthanides. Yb, Y, and lutetium (Lu) are the leading candidates for use in RE silicate EBCs. SiC, mullite, β-RE₂Si₂O₇ (RE = Sc, Lu, Yb), and γ-Y₂Si₂O₇ all have a CTE of ~4.0x10⁻⁶ K⁻¹ as demonstrated in Figure 8 [12], [13]. Lu silicates lack polymorphs but are undermined by SiO₂ present on grain boundaries after deposition. The SiO₂ is readily volatilized in expected operation conditions [13]. Y, thulium (Tm), erbium (Er), and holmium (Ho) disilicates have several polymorphs with disparity in density which makes them unsuitable with thermal cycling [12].

Additionally, YbDS has lower silica volatility and closer CTE match with SiC compared to Y-monosilicate (YMS) [12], [13]. Therefore, YbDS is seen as the best RE silicate candidate for RE EBC applications. Current EBC systems still face several challenges including issues with chemical compatibility, CTE mismatch, delamination, premature failure under service conditions, stability of the bond coating, and CMAS attack [12]. Additionally, there is a lack of theoretical criterion to judge EBC performance, and the complexities of a real-world working environment are not adequately captured through available testing setups.

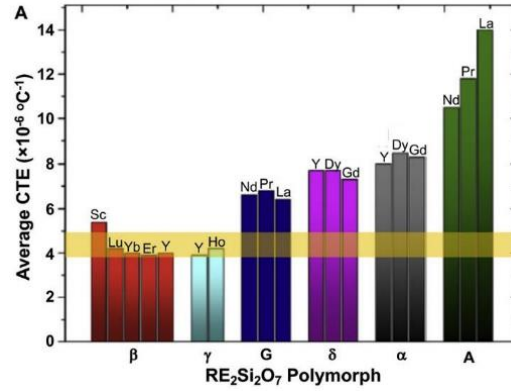


Figure 8: A comparison of several RE disilicate polymorphs. The yellow bar indicates the effective CTE of SiC [13].

Residual Stresses: Ye and Jiang do mention the importance of residual stresses and their consequences. However, no explanation is offered on the causes of these stresses and the mechanisms behind the failures mentioned. Additionally, there is little explanation behind the Poisson effect and its relation to biaxial stresses. There are two primary sources of stress/strain present in a defect free as-deposited coating system: lattice misfit and thermal misfit. Lattice misfit strain occurs when there is a dissimilarity between the lattice spacing, d , of a coating and its substrate [46], [57]. Thermal strain is a result of CTE mismatch between substrate and coating. During the deposition process, both substrate and coating are heated causing volumetric expansion. Upon cooling, both components contract. If the two components have different CTE values, they will have different dimensions in their unheated state. However, since they are bound together, they must accommodate one another. The dimensional difference between the bound and unbound state is the thermal strain. For a coating, the thermal strain and stress can be calculated through the following equations [31], [41], [57]:

$$\varepsilon_t = (\alpha_c - \alpha_s)\Delta T \quad (8)$$

$$\sigma_t = \frac{E_c}{1 - \nu_c}(\alpha_c - \alpha_s)\Delta T \quad (9)$$

Here, ε_t represents the thermal strain, σ_t the stress, α is the CTE, ΔT is the difference in temperature, E is the Elastic modulus, and ν is Poisson's ratio. The subscripts c and s stand for coating and substrate, respectively. If the CTE of the coating is greater than CTE of the substrate, the coating will experience tensile stress. If $\alpha_s > \alpha_c$, the coating will experience compressive stress.

Actual coating systems are not defect free and usually undergo significant thermal cycling during use. The residual stress in these coatings is therefore a combination of three things: thermal cycle stress, intrinsic stress, and aging stress [31], [41], [46]. Intrinsic stress is a result of the deposition process and includes the original thermal mismatch, the lattice mismatch, and other defects created during deposition [31], [41], [46]. Intrinsic stress may also be referred to as growth stress. Aging stress is the result of changes in physical, mechanical, and chemical properties induced by thermal exposure [31]. These may be caused by phase transformations, sintering, oxidation, and other chemical reactions. The total residual stress, where σ_{in} is the intrinsic stress and σ_a is the aging stress, is therefore given by:

$$\sigma = \sigma_t + \sigma_{in} + \sigma_a \quad (10)$$

Defects, such as micropores, act as stress concentrators [58]. Micropores may coalesce into microcracks which grow depending on the residual stress [42]. Under dynamic cyclic stress or strain, like that present during thermal cycling, crack growth is given by Equations 11 & 12:

$$\frac{da}{dN} \sim A(\Delta K)^p \quad (11)$$

$$K \approx Y\Delta\sigma(\pi a)^{0.5} \quad (12)$$

Here, a is the crack length, N is the number of cycles, ΔK is the cyclic range of stress intensity factors, p and A are constants, Y is a constant dependent on crack geometry, and $\Delta\sigma$ is the range of stresses [58]. In addition to the formation of cracks, buckling of the TGO or intermediate layers may occur. Buckling occurs when an initially flat layer lowers its strain energy by adopting a rumpled geometry [17]. This is particularly problematic in the TGO layer because the TGO may undergo phase changes during thermal cycling [18]. If the topcoat, or other layers, cannot accommodate dimensional changes in the buckled layer, they may separate [17]. This separation may lead to the formation of voids or delamination. An example of buckling and a cracked EBC is depicted in Figure 9.

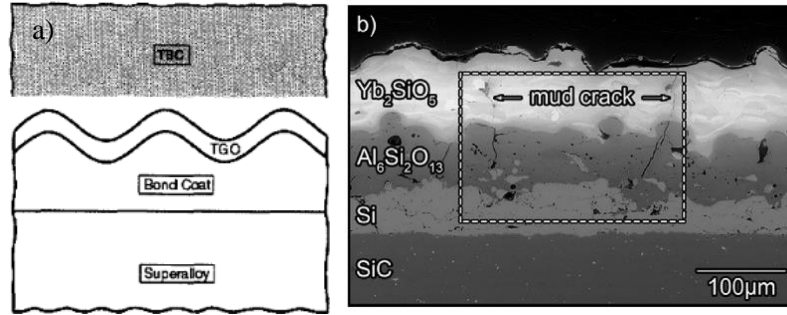


Figure 9: a) An example of TGO buckling between a bond coat and TBC [17]. b) A RE monosilicate EBC demonstrating mud cracks which penetrate the topcoat and intermediate layers [18].

In an isotropic material, the strain in a certain direction, x , can be determined through Poisson relations to the stress in other principle directions, y and z , through:

$$\epsilon_x = \frac{1}{E} (\sigma_x - \nu(\sigma_y + \sigma_z)) \quad (13)$$

Here, all variables have similar meaning to those used in previous equations. The stress in a thin film or coating at the free surface, or in the z direction, is typically negligible. Furthermore, through symmetry, the two in-plane stresses, are the same, $\sigma_x = \sigma_y = \sigma_b$.

$$\therefore \epsilon_x = \frac{1}{E} (\sigma_b - \nu\sigma_b) = \frac{\sigma_b}{E} (1 - \nu) \Rightarrow \frac{\sigma_b}{\epsilon_x} = \frac{E}{1 - \nu} = E_b \quad (14)$$

E_b is the biaxial modulus and σ_b represents the biaxial stress. This biaxial stress effect, which is basically the Poisson effect, can be used to determine the in-plane stress based on the measured stress along a free edge, σ_e [32], [59]:

$$\epsilon_x E = \sigma_x = \sigma_e \therefore \sigma_b = \frac{\sigma_e}{1 - \nu} \quad (15)$$

The $\text{Sin}^2 \Psi$ Method: An important consideration of the $\text{Sin}^2 \Psi$ method is neglected in their study. The $\text{Sin}^2 \Psi$ method requires a high diffraction angle, usually $2\theta > 125^\circ$, to reduce error [40]. In contrast, stress can be measured using Glancing Incident XRD (GIXRD). GIXRD uses a constant low Ω , and the diffraction peaks are measured by varying the angle between the detector and substrate. This is useful for measuring residual stress of extremely thin films because the penetration depth of the X-rays is much lower [40]. Because angles of incidence are different for each plane, the penetration depth of the X-rays are different for each measurement, and therefore the volume measured for stress is different too. This means that

“measured residual stress is an approximate estimation of the overall residual stress instead of an accurate measurement” [40].

Raman Piezospectroscopy: The generation of a Raman spectrum is also never fully explained, making the reader seek further background information. During Raman spectroscopy, a laser emitting light with frequency f_0 is reflected off a sample. The reflected light is either elastically or inelastically scattered. Elastic scattering is called Rayleigh scattering while inelastic scattering is called Raman scattering [60]. During Raman scattering, light momentarily interacts with a molecule causing transitions between vibrational levels [60], [61]. This interaction causes a change in the frequency of the scattered photons. This new frequency is given by:

$$f = f_0 \pm f_m \quad (16)$$

f_m corresponds to the change in vibrational energy of the molecule. After reflection, the light is collected by an objective lens, the contribution from Rayleigh scattering is filtered using a notch or edge filter, and the remaining Raman-scattered light is then separated into different wavenumbers. In spectroscopy, wavenumber is given by:

$$\nu' = \frac{1}{\lambda} = \frac{f}{c} \quad (17)$$

In this equation, c is the speed of light, λ is the wavelength. ν' is given in units of inverse length (cm^{-1} typically). In spectroscopic applications, the term wavenumber and frequency are often used interchangeably. A Raman shift is obtained when the wavenumber of a scattered photon is subtracted from the wavenumber of the photons generated by the laser, ν_l' . A Raman spectrum is generated when the intensity of the Raman-scattered light is plotted against its Raman shift [60], [61]. The Raman shift is defined as:

$$RS = \nu = \nu_l' - \nu' = \frac{1}{c}(f_0 - f) = \frac{1}{\lambda_l} - \frac{1}{\lambda} \quad (18)$$

Ye and Jiang also fail to consider that the PS coefficient demonstrates a dependency on the method which stress is applied, i.e. uniaxial (u), biaxial (b), or hydrostatic (h) stress. This failure may lead to an inaccuracy in their work discussed later. The PS coefficient of each case is related as follows [50], [51], [54], [55]:

$$\Pi_h = \frac{3}{2} \Pi_b = 3\Pi_u \quad (19)$$

Reproducibility

The purpose of scientific writing is to convey discoveries in a verifiable and reproducible way. This makes it important to report values used in calculations, as well as numerical values obtained that are pertinent for the interpretation of results. For example, the value of the Poisson ratio, ν , is required for the calculation of stress in the $\text{Sin}^2 \Psi$ method and the determination of the biaxial stress from the edge stress correction. Additionally, the $\text{Sin}^2 \Psi$ method requires Young’s modulus, E , to determine the surface stress. Neither Young’s modulus nor Poisson’s ratio were reported anywhere in the work of Ye and Jiang, making it extremely difficult to verify their calculations. Error in measurements is also important to report. In Figure 2 of their work (also Figure 2 in this work) no standard deviation or error is reported on either their measurements or the fitting itself. Similarly, the plot of the Raman peaks (their Figure 3) displays the fitting which they used, but they never report any numerical error associated with this fitting. Likewise, the actual stress value which they determined from the $\text{Sin}^2 \Psi$ plot and the calculated PS coefficient are both absent.

In the final paragraph of their *Experimental Results and Discussion* section, a calculation of the penetration depth of the X-rays is performed. This is to ensure the X-ray penetration is similar to the first Raman peak measurement depth. They determine that it is similar using a relationship for the linear attenuation coefficient: $\mu \approx k\rho Z^3 \lambda^3$. Here they explain that ρ is the density, Z is the atomic number of the material, and λ is the wavelength of the X-ray. There is no reference or justification given for this relationship, and the variable k is never explained. Furthermore, the values they used for this equation are not reported. These

values are not straightforward either because this material is composed of several different elements, and the wavelength of the X-ray is never specified in the article.

The conditions and specifics of the slurry coating process are also missing. This makes the experiment in this article essentially impossible to reproduce. It was mentioned earlier that the residual stress in coatings is a combination of thermal stress, intrinsic stress, and aging stress [31], [41], [46]. Intrinsic stress is a result of the deposition process, so without description of this process, their work can never be reliably reproduced for the same type of samples.

Accuracy

Scientific works must be accurate to serve as reliable resources. There are few signs of overt inaccuracies in their work, but several key aspects require edification. The residual stress reported in the YbDS topcoat falls in the range of -140 to -300 MPa. The negative sign indicates that a compressive stress is present. This magnitude of stress is not unexpected because stresses up to several GPa may be present in coating layers [21], [41]. However, the claim of compressive stress should be considered carefully. Ye and Jiang claim, “All peak shifts were positive in the top coat, indicating that the entire coating was subjected to compressive stress.” A positive peak shift is not always necessary to demonstrate compressive stress as evidenced in the work of Bouvier and Lucazeau [52]. Additionally, the presence of micropores within the YbDS coating (Figure 1 of their work and Figure 1 here) seem to suggest that a tensile stress may be present. This effect would be akin to the formation of microcracks discussed earlier. Conversely, the presence of micropores in the TGO layer and the $\text{Sin}^2 \Psi$ measurement do support their claims of compressive stress. If the TGO layer is in tension, it is likely that the YbDS topcoat is in compression as the two layers would exert opposite stresses on one another. Regardless, they have no way to validate that their method is accurately measuring the stress throughout the profile. The XRD measurements may support the values near the top of the coating, but there is no way to demonstrate the accuracy of their measurements further from the coating surface. They claimed that their results were consistent with the work of Richards et al., which used a finite element method to determine stress magnitude [18]. This could be problematic because models often have significant error [43]. Claiming validity of a measurement based on results of model calculations is not always the soundest practice.

The use of the low diffraction angle for the $\text{Sin}^2 \Psi$ method ($2\theta = 47.700$) is interesting. Usually a higher diffraction angle ($2\theta > 125^\circ$) is selected during the $\text{Sin}^2 \Psi$ method so that the substrate planes are not also sampled [40]. They cited the need for lower 2θ so that the area of the XRD scan would not be expanded by a higher diffraction angle. If this was a concern, the GIXRD method should have been employed. The claim that the coating exhibited “good protective performance” due to the lack of observed cracks must be more rigorously proven too. The actual simulation of the high-temperature corrosive environment is significantly different than the testing that other similar coating systems are subjected to. Often, the coated samples are subject to a flowing atmosphere consisting of up to 90% H_2O vapor and 10% O_2 with several cycles of high temperature [18], [31], [35], [36]. Additionally, silica or silica forming tubes cause high internal $P_{\text{Si(OH)}_4}$ (silicon hydroxide partial pressure), and alumina tubes cause higher $P_{\text{Al(OH)}_3}$ [12]. This could artificially slow corrosion rates. Since Ye and Jiang use an alumina tube, they should be cognizant of this fact.

An overt inaccuracy in the work of Ye and Jiang can be found in the first and second paragraph of the *Experimental results and discussion* section. These paragraphs are quoted in Appendix A for convenience. Ye and Jiang claim that Equation 1 (in the present work) is defined for only cubic crystal systems by Bouvier and Lucazeau [52]. This same equation is used in the work of Krämer et al. for polycrystalline zirconia – not only cubic crystalline structures [59]. Equation 1 is more accurately described as Equation 20. Where the stress terms describe the average of the hydrostatic pressure and the Π term is divided by three to represent a uniaxial stress compared to the hydrostatic pressure [59]:

$$\Delta v_n = \frac{\Pi_n \langle \sigma_1 + \sigma_2 + \sigma_3 \rangle}{3} \quad (20)$$

At the beginning of the second paragraph, Ye and Jiang indicate that YbDS is monoclinic. This is indeed the case [62]. However, they later state, “Considering that the distinctive minimal lattice distortion of the silicon-oxygen tetrahedron structure is observed in YbDS crystals due to its high structural stiffness [23], the cubic structure of YbDS facilitated the calculation of residual stress through Equation (1).” Claiming cubic structure in this sentence is false and a contradiction. Additionally, Ye and Jiang claim that the 921 cm^{-1} peak in the Raman spectrum corresponds to Si-O-Si bending vibrations. Their reference 22, by Zheng et al., clearly states that the 500-700 cm^{-1} peaks are attributed to the distorting bending vibration in $(\text{SiO}_4)^{4-}$ tetrahedron [63]. Zheng et al. indicate that the peaks in the 800-1000 cm^{-1} range are attributed to symmetric and antisymmetric stretching instead.

Novelty & Impact

Ye and Jiang also claim that by coupling the $\text{Sin}^2 \Psi$ method with Raman piezospectroscopy, they have developed a novel method. This may be the first time which these two methods were explicitly coupled to calculate the PS coefficients, but it is not the first time in which such a coupling was suggested, nor was it the first time that the stress measured from XRD was correlated to stress measured in Raman piezospectroscopy. In a study by Constable et al., TiAlN/VN coatings were deposited on stainless steel substrates [41]. The deposition parameters were varied between samples resulting in residual stresses that caused peak shifts in the Raman spectra. In their study, the peak shifts were then correlated to the residual stress measured by the GIXRD $\text{Sin}^2 \Psi$ method. In a separate study by Tomaszewski et al., a method for indirectly determining the PS coefficient without calibration is proposed [54]. If a sample is composed of two different constituents, it satisfies the equilibrium condition:

$$f_1 \langle \sigma \rangle_1 + f_2 \langle \sigma \rangle_2 = 0 \quad (21)$$

Here, f is the volume fraction of one of the constituents and $\langle \sigma \rangle$ is the average stress in that material. Through some simple algebra, the PS coefficient of one of the materials can be determined as follows:

$$\Pi_2 = -\frac{f_2 \Delta \nu_2}{f_1 \langle \sigma \rangle_1} \quad (22)$$

Essentially, if the average stress of one material is known, the PS coefficient of the secondary material can be calculated based on its peak shift, $\Delta \nu$, and the volume fractions. This study demonstrates that the work of Ye and Jiang is not the first attempt to indirectly measure the PS coefficient without calibration. Finally, the work of Loechele et al. represents another method which can be used to determine stress using Raman spectroscopy without prior knowledge of the PS coefficients [64]. Basically, by polarizing the laser light and setting the detector off axis, meaning it is not in line with the reflection, the setup could sample different Raman active phonons, and therefore be used to determine the exact nature of the stress tensor.

Unfortunately, the proposed method of Ye and Jiang suffers another drawback. Their method still requires sectioning of a sample to access the cross-sectional area. This makes the method destructive and not immediately applicable for in-situ measurements. A promising improvement could be made if the confocal nature of many Raman microscopes could be utilized. Basically, a confocal microscope can focus at different depths within a sample. This means that the stress at different depths could be measured much like the work of Ohtsuka et al. [50]. They measured the residual stress along the depth of CVD deposited Al_2O_3 coatings on a Si_3N_4 substrates through confocal Raman piezospectroscopy without cutting their samples. This was possible because the Al_2O_3 coatings are relatively transparent to the laser. So, the overall impact and usefulness of Ye and Jiang’s work could be improved if they took advantage of the confocal nature of certain microscopes.

Suggested Improvements

There are several ways in which the work of Ye and Jiang can be improved. First, the values used in all calculations should be reported – Poisson’s ratio, Young’s modulus, the stress determined from the XRD measurement, and the calculated PS coefficient. This would greatly enhance the reproducibility of their work and allow readers to develop logical conclusions. Some form of validation is also necessary. Since

this work represents an underutilized coupling method, it is important to establish its validity. This could be done through determination of the PS coefficients through a calibration sample, or the method may be applied to well-studied materials. A well-studied material, like YSZ, has widely reported PS coefficient values and coating deposition mechanisms. If Ye and Jiang apply their method to such a material, their results would be immediately comparable to other works. Similarly, because residual stress varies with deposition parameters, it is important to report details on the coating procedures. This would allow for other researchers to reproduce the results as well as build off the proposed method.

An accurate comparison of the as-deposited to tested samples would also be beneficial. This may take the form of accurately measuring the thickness of the EBC samples or taking an SEM image prior to the heat treatment/corrosion test. This would give better insight into the development of the microstructure under these testing conditions, and it would quantitatively characterize the coating performance. The paper could also be improved by showing the entire Raman spectrum – of both the powder YbDS and coated YbDS. It also would have been more appropriate to pick a peak that was not convoluted with another peak. This would reduce the error and is typically not difficult. The overall organization of the paper can also be improved. In several paragraphs, the figures are referred to well after they are shown - often on a different page. The figures also leave an unnecessary amount of white space. This makes the figures difficult to reference and the article hard to read. This may be out of the authors' control due to journal policy but fixing this issue would improve the article overall. In terms of consistency, the authors claim to use Lorentz fitting and Lorenz fitting. These are two different equations with different uses developed by different people. The authors should make sure that the correct fitting equation is specified throughout the paper.

There are a few further considerations which Ye and Jiang should make. The article may be easier to understand if a diagram showing residual stresses and the coordinates of the XRD measurements are included such as in Figure 5 and reference [32]. Depending on the spatial resolution of the XRD measurements, Ye and Jiang may consider taking stress measurements along the depth using the $\sin^2 \Psi$ method much like they did with Raman spectroscopy. This could serve as an effective calibration method. Additionally, BSAS is known to go through a phase transition at high temperatures (1590 °C) [31], [43]. This high temperature phase may be present due to deposition conditions, and it is known to persist for long periods of time below the transition temperature. Since the EBC used in Ye and Jiang's work contains BSAS, this phase transition should be considered. Finally, the possibility of chemical reaction between the coating precursors should be considered. If the precursors (YbDS and BSAS) had undergone a chemical reaction to form a material with indistinct grains during the coating process, it would be difficult to obtain the unstressed Raman spectrum for comparison using the proposed method.

Conclusions

Ceramic matrix composites (CMCs) combined with environmental barrier coatings (EBCs) offer promising solutions for structural components in a wide swath of high temperature applications. Unfortunately, the deposition process, difference in coefficients of thermal expansion, and environmental conditions create residual stresses in these coatings, limiting their lifetime and capability. Thus, measurement of residual stresses is crucial. The work of Ye and Jiang does present a promising application of Raman Spectroscopy and XRD which could simplify and expedite the measurements of residual stresses in EBCs or other protective coatings. Their work serves as an important steppingstone in establishing reliable lifetime and performance models of EBCs. Several issues involving reproducibility and accuracy do exist in their work. These can be improved by the incorporation of a validation method and reporting of pertinent parameters used in calculation and EBC deposition.

Appendix A

First and second paragraph of the *Experimental results and discussion* section from Ye and Jiang [22]. References cited in the quotation are those of their article and not the present work.

“The microstructure of the YbDS/BSAS top coat after heat treatment is presented in Fig. 1b. The top coat is thinner than a typical TBC, with a uniform surface covered with bright and grey areas. Importantly, no large cracks were observed, which indicated the good protective performance of the coating. Moreover, the darker TGO layer is visible in the SEM image.

The distribution of residual stress through the thickness of coatings has been measured by Raman piezo-spectroscopy. For cubic crystal systems, the relationship between stress and peak shifts can be expressed as follows [21]:

$$\Delta\nu_n = \frac{\Pi_n(\sigma_1 + \sigma_2 + \sigma_3)}{3} \quad (1)$$

where the subscript n refers to the Raman peak, and v refers to peak shifts. However, the crystal structure of YbDS belongs to the monoclinic system instead of the cubic crystal system. Many well formed, symmetrical peaks with high intensity and a narrow FWHM (i.e. full width at half maximum) appeared in the spectrum. According to previous literature [22], the peak with the highest intensity at approximately 921 cm^{-1} corresponds to the characteristic peak of Si–O–Si bend vibration in a silicon-oxygen tetrahedron. Considering that the distinctive minimal lattice distortion of the silicon-oxygen tetrahedron structure is observed in YbDS crystals due to its high structural stiffness [23], the cubic structure of YbDS facilitated the calculation of residual stress through Equation (1). Here, we observed a significant linear relationship between the characteristic peak shift at 921 cm^{-1} and the applied stress.”

References

- [1] S. Bose, "Introduction," in *High Temperature Coatings*, vol. 12, no. 1, Elsevier, 2018, pp. 1–6.
- [2] L. K. Mansur, A. F. Rowcliffe, R. K. Nanstad, S. J. Zinkle, W. R. Corwin, and R. E. Stoller, "Materials needs for fusion, Generation IV fission reactors and spallation neutron sources - Similarities and differences," *J. Nucl. Mater.*, vol. 329–333, no. 1-3 PART A, pp. 166–172, 2004.
- [3] S. X. Mao, "Impermeable thin Al₂O₃ overlay for TBC protection from sulfate and vanadate attack in gas turbines," Pittsburgh, PA, 2003.
- [4] "Materials for Harsh Service Conditions Chapter 6: Technology Assessments," 2015.
- [5] F. García Ferré *et al.*, "Radiation endurance in Al₂O₃ nanoceramics," *Sci. Rep.*, vol. 6, no. September, pp. 1–10, 2016.
- [6] Y. Ueki, T. Kunugi, M. Kondo, A. Sagara, N. B. Morely, and M. A. Abdou, "Consideration of Alumina Coating Fabricated by Sol-gel Method as MHD Coating against PbLi," in *Proceedings of the 13th International Topical Meeting on Nuclear Reactor Thermal Hydraulics*, 2009, pp. 1–10.
- [7] M. Nuri Rahuma and B. Kannan M, "Corrosion in Oil and Gas Industry: A Perspective on Corrosion Inhibitors," *J. Mater. Sci. Eng.*, vol. 03, no. 03, p. 4172, 2014.
- [8] M. Belmonte, "Advanced ceramic materials for high temperature applications," *Adv. Eng. Mater.*, vol. 8, no. 8, pp. 693–703, 2006.
- [9] A. Hasegawa, A. Kohyama, R. H. Jones, L. L. Snead, B. Riccardi, and P. Fenici, "Critical issues and current status of SiC/SiC composites for fusion," *J. Nucl. Mater.*, vol. 283, no. 287, pp. 128–137, 2000.
- [10] V. Rubio *et al.*, "Thermal properties and performance of carbon fiber-based ultra-high temperature ceramic matrix composites (Cf-UHTCMCs)," *J. Am. Ceram. Soc.*, vol. 103, no. 6, pp. 3788–3796, 2020.
- [11] R. Raj, "Fundamental Research in Structural Ceramics for Service Near 2000°C," *J. Am. Ceram. Soc.*, vol. 76, no. 9, pp. 2147–2174, 1993.
- [12] Y. Xu, X. Hu, F. Xu, and K. Li, "Rare earth silicate environmental barrier coatings: Present status and prospective," *Ceram. Int.*, vol. 43, no. 8, pp. 5847–5855, 2017.
- [13] T. H. Daniel Tejero-Martin, Chris Bennett, "A Review on Environmental Barrier Coatings: History, Current State of the Art and Future Developments," 2020.
- [14] H. Ohnabe, S. Masaki, M. Onozuka, K. Miyahara, and T. Sasa, "Potential application of ceramic matrix composites to aero-engine components," *Compos. Part A Appl. Sci. Manuf.*, vol. 30, no. 4, pp. 489–496, 1999.
- [15] K. K. Chawla, "Ceramic Matrix Composites," in *Composite Materials*, vol. 43, no. 4, Cham: Springer International Publishing, 2019, pp. 251–296.
- [16] S. Bose, "Thermal Barrier Coatings (TBCs)," in *High Temperature Coatings*, Elsevier, 2018, pp. 199–299.
- [17] D. R. Clarke and C. G. Levi, "Materials Design for the Next Generation Thermal Barrier Coatings," *Annu. Rev. Mater. Res.*, vol. 33, no. 1, pp. 383–417, Aug. 2003.
- [18] B. T. Richards, S. Sehr, F. De Franqueville, M. R. Begley, and H. N. G. Wadley, "Fracture mechanisms of ytterbium monosilicate environmental barrier coatings during cyclic thermal

- exposure,” *Acta Mater.*, vol. 103, pp. 448–460, 2016.
- [19] K. N. Lee, “Current status of environmental barrier coatings for Si-based ceramics,” *Surf. Coatings Technol.*, vol. 133–134, pp. 1–7, 2000.
 - [20] V. Teixeira, M. Andritschky, W. Fischer, H. P. Buchkremer, and D. Stöver, “Analysis of residual stresses in thermal barrier coatings,” *J. Mater. Process. Technol.*, vol. 92–93, pp. 209–216, 1999.
 - [21] Y. H. Sohn, B. Jayaraj, S. Laxman, B. Franke, J. W. Byeon, and A. M. Karlsson, “The non-destructive and nano-microstructural characterization of thermal-barrier coatings,” *JOM*, vol. 56, no. 10, pp. 53–56, Oct. 2004.
 - [22] C. Ye and P. Jiang, “Accurate residual stress measurement as a function of depth in environmental barrier coatings via a combination of X-ray diffraction and Raman spectroscopy,” *Ceram. Int.*, vol. 46, no. 8, pp. 12613–12617, 2020.
 - [23] A. Sommers, Q. Wang, X. Han, C. T’Joen, Y. Park, and A. Jacobi, “Ceramics and ceramic matrix composites for heat exchangers in advanced thermal systems-A review,” *Appl. Therm. Eng.*, vol. 30, no. 11–12, pp. 1277–1291, 2010.
 - [24] J. Cho, A. R. Boccaccini, and M. S. P. Shaffer, “Ceramic matrix composites containing carbon nanotubes,” *J. Mater. Sci.*, vol. 44, no. 8, pp. 1934–1951, 2009.
 - [25] D. Han, H. Mei, S. Xiao, K. G. Dassios, and L. Cheng, “A review on the processing technologies of carbon nanotube/silicon carbide composites,” *J. Eur. Ceram. Soc.*, vol. 38, no. 11, pp. 3695–3708, 2018.
 - [26] T. F. Cooke, “Inorganic Fibers-A Literature Review,” *J. Am. Ceram. Soc.*, vol. 74, no. 12, pp. 2959–2978, Dec. 1991.
 - [27] S. Schmidt, S. Beyer, H. Knabe, H. Immich, R. Meistring, and A. Gessler, “Advanced ceramic matrix composite materials for current and future propulsion technology applications,” *Acta Astronaut.*, vol. 55, no. 3–9, pp. 409–420, 2004.
 - [28] M. Klaus, C. Genzel, and H. Holzschuh, “Residual stress depth profiling in complex hard coating systems by X-ray diffraction,” *Thin Solid Films*, vol. 517, no. 3, pp. 1172–1176, 2008.
 - [29] E. Alat, A. T. Motta, R. J. Comstock, J. M. Partezana, and D. E. Wolfe, “Ceramic coating for corrosion (c3) resistance of nuclear fuel cladding,” *Surf. Coatings Technol.*, vol. 281, pp. 133–143, 2015.
 - [30] B. Fotovvati, N. Namdari, and A. Dehghanghadikolaei, “On Coating Techniques for Surface Protection: A Review,” *J. Manuf. Mater. Process.*, vol. 3, no. 1, p. 28, 2019.
 - [31] K. N. Lee, J. I. Eldridge, and R. C. Robinson, “Residual stresses and their effects on the durability of environmental barrier coatings for SiC ceramics,” *J. Am. Ceram. Soc.*, vol. 88, no. 12, pp. 3483–3488, 2005.
 - [32] M. Tanaka, R. Kitazawa, T. Tomimatsu, Y. F. Liu, and Y. Kagawa, “Residual stress measurement of an EB-PVD Y₂O₃-ZrO₂ thermal barrier coating by micro-Raman spectroscopy,” *Surf. Coatings Technol.*, vol. 204, no. 5, pp. 657–660, 2009.
 - [33] S. Ramasamy, S. N. Tewari, K. N. Lee, R. T. Bhatt, and D. S. Fox, “Environmental durability of slurry based mullite-gadolinium silicate EBCs on silicon carbide,” *J. Eur. Ceram. Soc.*, vol. 31, no. 6, pp. 1123–1130, 2011.
 - [34] S. Ramasamy, S. N. Tewari, K. N. Lee, R. T. Bhatt, and D. S. Fox, “EBC development for hot-

- pressed Y₂O₃/Al₂O₃ doped silicon nitride ceramics,” *Mater. Sci. Eng. A*, vol. 527, no. 21–22, pp. 5492–5498, 2010.
- [35] S. Ramasamy, S. N. Tewari, K. N. Lee, R. T. Bhatt, and D. S. Fox, “Slurry based multilayer environmental barrier coatings for silicon carbide and silicon nitride ceramics - I. Processing,” *Surf. Coatings Technol.*, vol. 205, no. 2, pp. 258–265, 2010.
 - [36] S. Ramasamy, S. N. Tewari, K. N. Lee, R. T. Bhatt, and D. S. Fox, “Slurry based multilayer environmental barrier coatings for silicon carbide and silicon nitride ceramics — II. Oxidation resistance,” *Surf. Coatings Technol.*, vol. 205, no. 2, pp. 266–270, Oct. 2010.
 - [37] J. I. Federer, “Alumina base coatings for protection of SiC ceramics,” *J. Mater. Eng.*, vol. 12, no. 2, pp. 141–149, Jun. 1990.
 - [38] T. Suetsuna, M. Ishizaki, M. Ando, N. Kondo, T. Ohji, and S. Kanzaki, “Lutetium disilicate coating on silicon nitride for high temperature oxidation resistance,” *J. Ceram. Soc. Japan*, vol. 112, no. 1305, pp. 301–304, 2004.
 - [39] D. D. Jayaseelan, S. Ueno, T. Ohji, and S. Kanzaki, “Sol-gel synthesis and coating of nanocrystalline Lu₂Si₂O₇ on Si₃N₄ substrate,” *Mater. Chem. Phys.*, vol. 84, no. 1, pp. 192–195, 2004.
 - [40] Q. Luo and S. Yang, “Uncertainty of the X-ray Diffraction (XRD) $\sin^2 \psi$ Technique in Measuring Residual Stresses of Physical Vapor Deposition (PVD) Hard Coatings,” *Coatings*, vol. 7, no. 8, p. 128, Aug. 2017.
 - [41] C. P. Constable, D. B. Lewis, J. Yarwood, and W. D. Münz, “Raman microscopic studies of residual and applied stress in PVD hard ceramic coatings and correlation with X-ray diffraction (XRD) measurements,” *Surf. Coatings Technol.*, vol. 184, no. 2–3, pp. 291–297, 2004.
 - [42] P. Jiang, X. Fan, Y. Sun, H. Wang, L. Su, and T. Wang, “Thermal-cycle dependent residual stress within the crack-susceptible zone in thermal barrier coating system,” *J. Am. Ceram. Soc.*, vol. 101, no. 9, pp. 4256–4261, 2018.
 - [43] B. J. Harder, J. D. Almer, C. M. Weyant, K. N. Lee, and K. T. Faber, “Residual stress analysis of multilayer environmental barrier coatings,” *J. Am. Ceram. Soc.*, vol. 92, no. 2, pp. 452–459, 2009.
 - [44] O. ANDEROGLU, “RESIDUAL STRESS MEASUREMENT USING X-RAY DIFFRACTION,” Texas A & M, 2004.
 - [45] S. Bose, “Nondestructive Inspection (NDI) of Coatings,” in *High Temperature Coatings*, Elsevier, 2018, pp. 301–318.
 - [46] I. A. Alhomoudi and G. Newaz, “Residual stresses and Raman shift relation in anatase TiO₂ thin film,” *Thin Solid Films*, vol. 517, no. 15, pp. 4372–4378, 2009.
 - [47] T. Tomimatsu, S. J. Zhu, and Y. Kagawa, “Local stress distribution in thermally-grown-oxide layer by near-field optical microscopy,” *Scr. Mater.*, vol. 50, no. 1, pp. 137–141, 2004.
 - [48] I. C. Noyan, T. C. Huang, and B. R. York, “Residual stress/strain analysis in thin films by X-ray diffraction,” *Crit. Rev. Solid State Mater. Sci.*, vol. 20, no. 2, pp. 125–177, Jan. 1995.
 - [49] Q. Chen, W. G. Mao, Y. C. Zhou, and C. Lu, “Effect of Young’s modulus evolution on residual stress measurement of thermal barrier coatings by X-ray diffraction,” *Appl. Surf. Sci.*, vol. 256, no. 23, pp. 7311–7315, 2010.
 - [50] S. Ohtsuka, W. Zhu, S. Tochino, Y. Sekiguchi, and G. Pezzotti, “In-depth analysis of residual stress in an alumina coating on silicon nitride substrate using confocal Raman piezo-spectroscopy,” *Acta*

- Mater.*, vol. 55, no. 4, pp. 1129–1135, 2007.
- [51] A. M. Limarga and D. R. Clarke, “Piezo-spectroscopic coefficients of tetragonal-prime yttria-stabilized zirconia,” *J. Am. Ceram. Soc.*, vol. 90, no. 4, pp. 1272–1275, 2007.
 - [52] P. Bouvier and G. Lucazeau, “Raman spectra and vibrational analysis of nanometric tetragonal zirconia under high pressure,” *J. Phys. Chem. Solids*, vol. 61, no. 4, pp. 569–578, 2000.
 - [53] W. G. Mao, Q. Chen, C. Y. Dai, L. Yang, Y. C. Zhou, and C. Lu, “Effects of piezo-spectroscopic coefficients of 8wt.% Y₂O₃ stabilized ZrO₂ on residual stress measurement of thermal barrier coatings by Raman spectroscopy,” *Surf. Coatings Technol.*, vol. 204, no. 21–22, pp. 3573–3577, 2010.
 - [54] H. Tomaszewski, J. Strzeszewski, L. Adamowicz, and V. Sergo, “Indirect Determination of the Piezospectroscopic Coefficients of Ceria-Stabilized Tetragonal Zirconia Polycrystals,” *J. Am. Ceram. Soc.*, vol. 85, no. 11, pp. 2855–2857, 2002.
 - [55] M. Tanaka, M. Hasegawa, A. F. Dericioglu, and Y. Kagawa, “Measurement of residual stress in air plasma-sprayed Y₂O₃-ZrO₂ thermal barrier coating system using micro-Raman spectroscopy,” *Mater. Sci. Eng. A*, vol. 419, no. 1–2, pp. 262–268, 2006.
 - [56] G. Pujol, F. Ansart, J.-P. Bonino, A. Malié, and S. Hamadi, “Step-by-step investigation of degradation mechanisms induced by CMAS attack on YSZ materials for TBC applications,” *Surf. Coatings Technol.*, vol. 237, pp. 71–78, Dec. 2013.
 - [57] J. Narayan, “Recent progress in thin film epitaxy across the misfit scale (2011 Acta Gold Medal Paper),” *Acta Mater.*, vol. 61, no. 8, pp. 2703–2724, 2013.
 - [58] S. Bose, “Fundamental Concepts,” in *High Temperature Coatings*, Elsevier, 2018, pp. 7–27.
 - [59] S. Krämer *et al.*, “Mechanisms of cracking and delamination within thick thermal barrier systems in aero-engines subject to calcium-magnesium-alumino-silicate (CMAS) penetration,” *Mater. Sci. Eng. A*, vol. 490, no. 1–2, pp. 26–35, 2008.
 - [60] J. R. Ferraro, K. Nakamoto, and C. W. Brown, “Basic Theory,” in *Introductory Raman Spectroscopy*, Elsevier, 2003, pp. 1–94.
 - [61] B. A. Kanies, “An investigation into the effects of ion tracks on α -quartz,” Missouri University of Science and Technology, 2018.
 - [62] K. Persson, “Materials Data on Yb₂Si₂O₇ (SG:12) by Materialsle,” 2016. [Online]. Available: <https://materialsproject.org/materials/mp-4300/>. [Accessed: 30-Aug-2020].
 - [63] L. Zheng *et al.*, “Raman spectroscopic investigation of pure and ytterbium-doped rare earth silicate crystals,” *J. Raman Spectrosc.*, vol. 38, no. 11, pp. 1421–1428, Nov. 2007.
 - [64] G. H. Loehelt, N. G. Cave, and J. Menéndez, “Polarized off-axis Raman spectroscopy: A technique for measuring stress tensors in semiconductors,” *J. Appl. Phys.*, vol. 86, no. 11, pp. 6164–6180, 1999.